2018

Evaporation of a sessile droplet on a slope

Mitch Timm
Michigan Technological University, mltimm@mtu.edu

EVAPORATION OF A SESSILE DROPLET ON A SLOPE

By

Mitchel L. Timm

A THESIS

Submitted in partial fulfillment of the requirements for the degree of

MASTER OF SCIENCE

In Mechanical Engineering

MICHIGAN TECHNOLOGICAL UNIVERSITY

2018

This thesis has been approved in partial fulfillment of the requirements for the Degree of MASTER OF SCIENCE in Mechanical Engineering.

Department of Mechanical Engineering-Engineering Mechanics

Thesis Advisor: *Dr. Hassan Masoud*

Committee Member: *Dr. Fernando Ponta*

Committee Member: *Dr. Song-Lin Yang*

Department Chair: *Dr. William W. Predebon*

Dedication

To my parents and siblings,

who supported me through many years of education, and who pushed me (forcibly) to strive for greater heights. Without all of them, I would not have had the will to continue this far, and be where I am today.

Acknowledgments

I would like to thank my advisor, Dr. Hassan Masoud, and colleagues at Michigan Tech, Esmaeil Dehdashti and Saeed Jafari Kang, for their invaluable help and advice in the completion of my thesis.

Contents

Acknowledgments . . . . . **iv**

List of Figures . . . . . **vii**

Nomenclature . . . . . **ix**

Abstract . . . . . **xi**

1 Introduction **1**

2 Shape of a droplet resting on an inclined substrate **6**

2.1 Problem statement 6

2.2 Analytical solution using a perturbation theory 8

2.3 Numerical solution based on energy minimization 13

2.4 Results and discussion 16

3 Quasi-steady evaporation of a non-axisymmetric sessile droplet **22**

3.1 Problem statement 22

3.2 Analytical solution using a perturbation theory 24

3.3 Numerical solution via a finite volume method 28

3.4 Results and discussion 30

4 Summary and future directions **33**

References **35**

List of Figures

1.1 Example of sessile drops on solar panels (Photo Credit: Oregon Department of Transportation). 2

2.1 (a) A stationary droplet on an inclined surface. (b) Side view of panel (a), where the inclination angle is denoted by α and the arrow shows the direction of the gravity vector $\boldsymbol{g}$. (c) Rotated, by $-\alpha$, view of panel (b). 8

2.2 (a) Initial and (b) converged geometry of sessile drop from the *Surface Evolver* with parameters Bo $= 5$, $\theta_c = \pi/2$, and $\alpha = \pi/6$. For visualization purposes the discretized mesh shown in (b) is coarser than what was actually used in our numerical analyses. 14

2.3 Center-line profiles of sessile drops for varying Bo and θ_c, while $\alpha = 0$ is constant. 17

2.4 Center-line profiles of sessile drops for varying Bo and θ_c, while $\alpha = \pi/6$ is constant. 18

2.5 Center-line profiles of sessile drops for varying Bo and θ_c, while $\alpha = \pi/3$ is constant. 19

2.6 Center-line profiles of sessile drops for varying Bo and θ_c, while $\alpha = \pi/2$ is constant. 20

3.1 Example of a multi-block grid used for numerically solving Laplace's equation outside a sessile droplet (shown in blue). For clarity, only surface meshes on the symmetry plane and substrate are shown. The grid is generated by the *snappyHexMesh* utility of *OpenFOAM* [41], and coarsen as the distance from the free surface of the drop increases. 29

3.2 Percent difference δ between our analytical and numerical models for (a) $\theta_c = \pi/6$, (b) $\theta_c = \pi/3$, (c) $\theta_c = \pi/2$, and (d) $\theta_c = 2\pi/3$. 31

3.3 Normalized total rate of evaporation for (a) $\theta_c = \pi/6$, (b) $\theta_c = \pi/3$, (c) $\theta_c = \pi/2$, and (d) $\theta_c = 2\pi/3$. 32

Nomenclature

c	Liquid vapor concentration
c_s	Saturation vapor concentration at the surface of the droplet
c_∞	Far-field vapor concentration
Bo	Bond number
g	Gravitational acceleration
H	Mean curvature
J	Rate of evaporation
r	Radial coordinate in spherical coordinate systems
$\boldsymbol{n}$	Normal unit vector
$P_{-1/2+i\tau}$	Conical function of the first kind
R	Contact line radius
$\mathcal{R}$	Function representing the free surface of the droplet
$\mathcal{R}_c$	Value of $\mathcal{R}$ at the contact line
$\mathcal{R}_{ax}^{(1)}$	Function representing axisymmetric deformation of the droplet under gravity
$\mathcal{R}_{nax}^{(1)}$	Function representing non-axisymmetric deformation of the droplet under gravity
S	Bounding surface of the volume occupied by liquid vapor
S_d	Free surface of the droplet

S_s	Surface of the substrate
S_0	Free surface of the unperturbed droplet
S_∞	Bounding surface at large distances
x	First component of the Cartesian coordinates
y	Second component of the Cartesian coordinates
z	Third component of the Cartesian coordinates
α	Inclination angle of the substrate
δ	Percent difference
γ	Surface tension
Γ	Level set function
ζ	Dummy variable
η	Dummy variable
θ	Polar angle coordinate in spherical coordinate systems
θ_c	Polar angle at the contact line
ν	Dummy variable
π	Pi number
ρ	Liquid density
τ	Dummy variable
ϕ	Relative vapor concentration field
φ	Azimuthal angle coordinate in spherical coordinate systems

Abstract

We theoretically examine the drying of a stationary liquid droplet on an inclined surface. Both analytical and numerical approaches are considered, while assuming that the evaporation results from a purely diffusive transport of the liquid vapor and that the contact line is a pinned circle. For the purposes of our analytical calculations, we suppose that the effect of gravity relative to the surface tension is weak, i.e. the Bond number (Bo) is small. Then, we express the shape of the drop and the vapor concentration field as perturbation expansions in terms of Bo. When the Bond number is zero, the droplet is unperturbed by the effect of gravity and takes the form of a spherical cap, for which the vapor concentration field is already known. Here, the Young-Laplace equation is solved analytically to calculate the first-order correction to the shape of the drop. Knowing the first-order perturbation to the drop geometry and the zeroth-order distribution of vapor concentration, we obtain the leading-order contribution of gravity to the rate of droplet evaporation by utilizing Green's second identity. The analytical results are supplemented by numerical calculations, where the droplet shape is first determined by minimizing the Helmholtz free energy, then the evaporation rate is computed by solving Laplace's equation for the vapor concentration field via a finite volume method. Perhaps counter-intuitively, we find that even when the droplet deforms noticeably under the influence of gravity, the rate of evaporation remains almost unchanged, as if no gravitational effect

is present. Furthermore, comparison between analytical and numerical calculations reveals that considering only the leading order corrections to the shape of the droplet and vapor concentration distribution provides estimates that are valid well beyond their intended limit of very small Bo.

Chapter 1

Introduction

Liquid droplets are ubiquitous in daily life, whether it is a spilled beverage on a table or morning dew on the hood of a car (see Fig. 1.1). Everyone has seen these quasi-spherical liquid forms and how they evaporate over time if left alone. Perhaps even, when driving while it is raining, one may have made the observation that the form of these drops change when on an inclined surface like a windshield. When on a slope, the seemingly spherical drops become more asymmetric with the majority of the volume shifted in the direction of the downward slope. A question that naturally arises from these observations is, how does the deformation of a droplet caused by gravity affect the rate of evaporation. The answer to this question is not only of general interest from a fundamental point of view, but is also of great relevance to the real-world applications that involve the drying of sessile droplets.

A large number of the applications that utilize the evaporation of sessile drops deal with colloidal suspensions that leave behind a residue once they completely dry out.

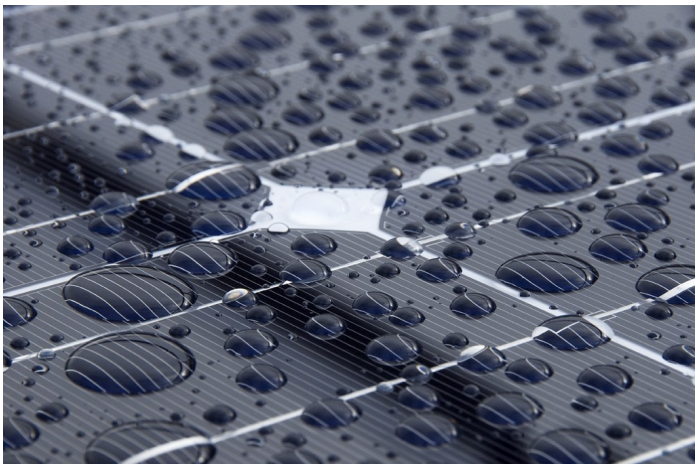

Figure 1.1: Example of sessile drops on solar panels (Photo Credit: Oregon Department of Transportation).

Common examples include ink-jet printing [1–6], fabricating ordered microelectronic structures via evaporative self-assembly [7–15], analysis of blood stain patterns for forensic and disease examination[16, 17], and fabrication of photovoltaic panels [18–20].

To date, the majority of studies on the evaporation of sessile drops have focused on axisymmetric geometries on horizontal substrates [21–26]. This simplification, however useful, is limiting, for in many practical situations, the droplets may rest on an incline. Among the small number of investigations that considered asymmetric sessile droplets, Espín and Kumar [27] and Du and Deegan [28] numerically examined the drying of (and the resulting flow field inside) two-dimensional colloidal droplets on inclined substrates. Also, Sáenz et al. [29] studied, both experimentally and numerically, the evaporation kinetics of non-axisymmetric drops placed on a flat surface and presented a general scaling law for the integrated evaporative flux. Lastly, Kim et al. [30] experimentally measured the lifetime and evaporation dynamics of water

droplets on slopes of various tilt angles. Overall, a close inspection of the literature indicates that our theoretical understanding of the effect of gravity on the evaporation of droplets on tilted substrates is incomplete. Attempting to partially fill the aforementioned knowledge gap, here, we theoretically analyze the drying of a sessile droplet on a slope.

Utilizing perturbation expansions coupled with known solutions for sessile drops on horizontal substrates [31, 32], we analytically derive a model for the shape of the deformed droplet while assuming the contact radius is a pinned circle. Starting from the Young-Laplace equation, we formulate a simple first-order expression that captures the asymmetric geometry of the drop in a spherical coordinate system. In our derivation, the Bond number Bo is used to relate the effects of gravity relative to the surface tension, allowing us to analyze the shape of the drop in dimensionless terms.

To supplement our analytical results we numerically calculate the shape of the perturbed drop using the same basic assumptions. Our numerical analysis uses an energy minimization method while enforcing the conservation of volume. Using this method, the angle of inclination is included by calculating the components of the gravitational potential normal and lateral to the substrate. This allows us to both bolster our analytical solution utilizing an independent method, and to analyze the drop evaporation with confidence in our geometries.

The total rate of evaporation is the final question we want to answer, and determine what effect the slope of the substrate has on this process. Similar to the calculation of the drop shape, we use a combination of analytical and numerical analysis to solve for the evaporation of the perturbed drop. In our analyses, we assume the evaporation is purely a result of the diffusive transport of liquid vapor, and that Bo is sufficiently small. Comparing our results ensures the accuracy of our analytical model for the rate of evaporation and provides keen insight into the relation to the slope of the substrate.

Our analytical derivation starts with the Laplace equation from our assumption of purely diffusive evaporation. Knowing the distribution for the concentration field of an axisymmetric drop [31], we use the first order correction to the drop shape coupled with Green's second identity to derive the leading-order contribution of gravity on the total rate of evaporation.

With the drop geometries generated and the same assumptions as our analytical derivation, we numerically calculate the total rate of evaporation using a finite volume method. Our numerical simulations are conducted by prescribing the vapor concentration on the surface of the drop as well as at infinity. These numerical calculations provide us with a solution for the rate of evaporation of the perturbed sessile drop with which we can confirm the accuracy of our analytical model.

Interestingly, we discover that even when the droplet geometry is significantly distorted by gravity, the rate at which the droplet loses mass changes only slightly.

This and other findings of our study provide additional insights into the evaporation of droplets on oblique planes. In the following chapters, we will first formulate the mathematical problem and describe its perturbation and numerical solutions. Then, we will present the results, discuss the implications, and provide a brief summary in the last chapter.

Chapter 2

Shape of a droplet resting on an inclined substrate

2.1 Problem statement

Our eventual goal is to show how the total rate of evaporation of a sessile drop is related to the Bond number and the slope of the substrate, however, the shape of the drop is an integral part of this problem and must first be discussed. The shape of a sessile drop is determined by several factors including its volume, the type of liquid involved, the wetting properties of the substrate, and any outside forces acting on the drop. In most of the previous studies, the substrate is assumed to be a horizontal plane, where gravity only acts normal to the surface. This assumption allows the drop to be considered axisymmetric. However, this simplification does not allow for the consideration of asymmetric geometries present in many real-world applications.

When the surface is tilted to some angle α, gravity no longer acts purely normal to the substrate, but instead contains a component that is parallel to the surface. This change means the drop is perturbed in the downward direction of the slope as shown in Fig. 2.1, and hence, α must also be considered while calculating the shape of the drop. The deformation of the droplet shape, in our case, is determined by two competing forces, surface tension and gravity. Depending on the volume of the drop and the angle of inclination, gravity will have a smaller or greater affect on the shape of the drop. This is why we derive all of our models, both for the drop shape as well as for the evaporation, in terms of the Bond number

$$\mathrm{Bo} = \frac{\rho g \mathcal{R}_c^2}{\gamma}, \tag{2.1}$$

where $\mathcal{R}_c$ is the radius of the spherical cap (see Fig. 2.1), ρ is the density of the liquid, g is the gravitational acceleration, and γ is the surface tension. The Bond number is a dimensionless parameter that relates the force of gravity to the surface tension.

It is well-known that the shape of a drop in the absence of gravity is a spherical cap. Knowing that, we can use perturbation theory to find the deviations in geometry induced by Bo and α to calculate the shape of the deformed drop while assuming the contact line is a pinned circle. To solve for the deformed shape of the drop, we analytically derive a model in spherical coordinates utilizing perturbation expansions. This allows us to describe the geometry (and eventually evaporation rate) of a sessile drop on a slope using a simple first-order expression. To supplement our analytical solution for the droplet shape, we also numerically compute the surface geometry

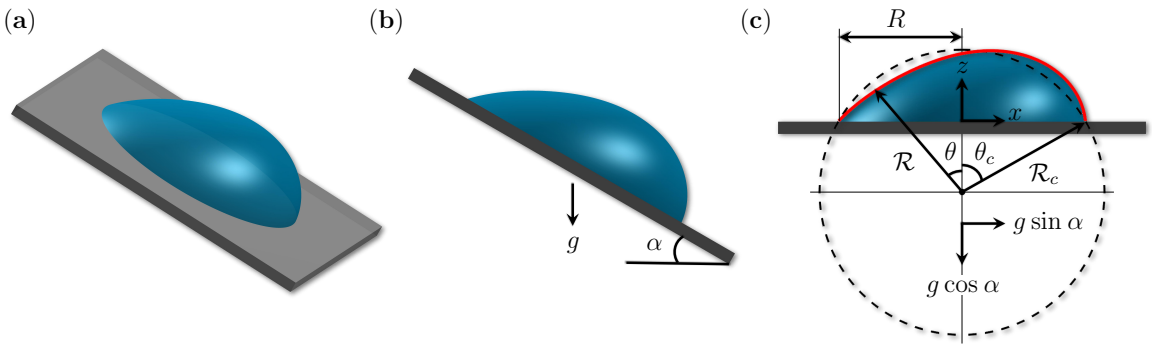

Figure 2.1: (a) A stationary droplet on an inclined surface. (b) Side view of panel (a), where the inclination angle is denoted by α and the arrow shows the direction of the gravity vector $\boldsymbol{g}$. (c) Rotated, by $-\alpha$, view of panel (b).

using an energy minimization method. Utilizing both of these methods provides us with additional confirmation of our results and insight into the conditions for which our analytical model is valid.

2.2 Analytical solution using a perturbation theory

Consider a static droplet (at room conditions) on a flat plate at angle α relative to the horizontal plane and suppose that the gravity acts in the downward vertical direction (see Figs. 2.1a and 2.1b). The equilibrium shape of the droplet is set by the force balance at the liquid-air interface, where the pressure difference across the interface is offset by the force of surface tension. Mathematically, the balance is expressed through the Young-Laplace equation

$$p - p_{atm} = \boldsymbol{\nabla} \cdot \boldsymbol{n} = -2H, \tag{2.2}$$

where p, p_{atm}, $\boldsymbol{n}$, and H denote the dimensionless hydrostatic pressure just below the interface, dimensionless atmospheric pressure, unit vector outward normal to the interface, and dimensionless mean local curvature, respectively [33]. In all of our analyses, pressure and length are nondimensionalized by $\gamma/\mathcal{R}_c$ and $\mathcal{R}_c$, respectively, where γ is the surface tension and $\mathcal{R}_c$ is a characteristic length of the droplet (see Fig. 2.1c). Equation 2.2 can also be derived from the minimum energy principle, which requires the equilibrium shape of the droplet to be the one that minimizes the Helmholtz free energy, subject to constant volume and other imposed constraints, if any [33].

Let (x, y, z) be the components of a Cartesian coordinate system with the origin at the center of the contact line, as depicted in Fig. 2.1c. The hydrostatic pressure can then be expressed as

$$p = p_0 - \mathrm{Bo}\, z \cos\alpha + \mathrm{Bo}\, x \sin\alpha, \tag{2.3}$$

where p_0 is the reference pressure at the origin.

In the absence of gravity (i.e. Bo = 0), p does not vary along the interface (irrespective of the tilt angle α) and, therefore, $\Delta p = p - p_{atm}$ becomes a constant. Hence, the mean curvature H is constant, meaning that the droplet takes the form of a spherical cap with a contact angle that depends on the wetting properties of the substrate. When the effect of gravity compared to that of surface tension is not negligible (i.e. Bo is finite), the hydrostatic pressure no longer stays uniform and, as

a result, the drop geometry deviates from a spherical cap. In general, Eq. 2.2 is challenging to solve analytically for arbitrary Bo. However, in situations where gravity is present, but weak (i.e. Bo $\ll 1$), the shape of the drop can be treated as a slightly perturbed spherical cap [34, 35]. In this limit, the Young-Laplace equation can be solved via a regular perturbation expansion in terms of Bo [35]. In the following, we describe the derivation.

To simplify the calculations, we follow previous studies [28, 35] and assume that the three-phase contact line is a pinned circle of radius R (see Fig. 2.1c). This condition is met, for example, when the droplet is initially deposited on a horizontal substrate (where it forms a pinned circular contact line) and then the substrate is gently tilted to an angle α. Considering that the unperturbed shape of the droplet is a spherical cap, it is more convenient to carry out the derivation in a spherical coordinate system whose components (r, θ, φ) are related to the Cartesian coordinates as

$$x = r\sin\theta\cos\varphi, \qquad y = r\sin\theta\sin\varphi, \qquad z = r\cos\theta - \cos\theta_c. \tag{2.4}$$

Here, $\mathcal{R}_c$ and θ_c, respectively, denote the values of r and θ at the contact line (see Fig. 2.1c), and are related to the volume of the droplet V and the radius of the contact line R via

$$V/\mathcal{R}_c^3 = (\pi/3)\,(2+\cos\theta_c)\,(1-\cos\theta_c)^2\,, \qquad R/\mathcal{R}_c = \sin\theta_c. \tag{2.5}$$

In (r, θ, φ) coordinates, the free surface of the droplet can be described as the zero level set of

$$\Gamma(r, \theta, \varphi; \mathrm{Bo}) = r - \mathcal{R}(\theta, \varphi; \mathrm{Bo}), \tag{2.6}$$

where $\mathcal{R}$ is the dimensionless shape function that we seek to determine for a given Bo. This function shall satisfy the condition $\mathcal{R}(\theta_c, \varphi; \mathrm{Bo}) = 1$ as well as the constraint that the volume enclosed between the free surface and the substrate be equal to V. Following Eq. 2.6, the right-hand side of Eq. 2.2 can be written as

$$\boldsymbol{\nabla} \cdot \boldsymbol{n} = -2H = \boldsymbol{\nabla} \cdot \frac{\boldsymbol{\nabla}\Gamma}{|\boldsymbol{\nabla}\Gamma|}. \tag{2.7}$$

Having set up the desired coordinate system, we now pose perturbation expansions as

$$\mathcal{R} = \mathcal{R}^{(0)} + \mathrm{Bo}\,\mathcal{R}^{(1)} + \mathcal{O}(\mathrm{Bo}^2), \tag{2.8a}$$

$$H = H^{(0)} + \mathrm{Bo}\,H^{(1)} + \mathcal{O}(\mathrm{Bo}^2), \tag{2.8b}$$

$$p_0 = p_0^{(0)} + \mathrm{Bo}\,p_0^{(1)} + \mathcal{O}(\mathrm{Bo}^2), \tag{2.8c}$$

which, upon substitution into Eq. 2.2 and the application of the pinned contact line condition, yield

$$p_0^{(0)} = p_{atm} - 2H^{(0)} \quad \text{with} \quad \mathcal{R}^{(0)}(\theta_c, \varphi) = 1, \tag{2.9a}$$

$$p_0^{(1)} = (\cos\theta - \cos\theta_c)\cos\alpha - \sin\theta\cos\phi\sin\alpha - 2H^{(1)} \quad \text{with} \quad \mathcal{R}^{(1)}(\theta_c, \varphi) = 0. \tag{2.9b}$$

Note that the reference pressure is not known *a priori* and is calculated as a part of the solution.

As discussed earlier, at the zeroth-order, we have

$$\mathcal{R}^{(0)} = 1, \quad H^{(0)} = -1, \quad p_0^{(0)} = p_{atm} + 2. \tag{2.10}$$

Replacing Eq. 2.8a for $\mathcal{R}$ in Eq. 2.6, while accounting for Eq. 2.10, and then substituting the result into Eq. 2.7, we obtain

$$H^{(1)} = \frac{1}{2}\left(\frac{\partial^2 \mathcal{R}^{(1)}}{\partial \theta^2} + \frac{1}{\sin^2\theta}\frac{\partial^2 \mathcal{R}^{(1)}}{\partial \varphi^2} + \frac{1}{\tan\theta}\frac{\partial \mathcal{R}^{(1)}}{\partial \theta} + 2\mathcal{R}^{(1)}\right) \tag{2.11}$$

for the first-order correction to the mean curvature of the interface. Equations 2.9b and 2.11 together constitute a partial differential equation (PDE) for $\mathcal{R}^{(1)}$. The linearity and structure of this PDE suggest a superposition solution in the form of

$$\mathcal{R}^{(1)}(\theta, \varphi) = \mathcal{R}^{(1)}_{ax}(\theta)\cos\alpha + \mathcal{R}^{(1)}_{nax}(\theta)\cos\varphi\sin\alpha, \tag{2.12}$$

where $\mathcal{R}^{(1)}_{ax}$ and $\mathcal{R}^{(1)}_{nax}$ represent the axisymmetric and non-axisymmetric deformation of the droplet, respectively, and satisfy the following ordinary differential equations:

$$\mathcal{R}^{(1)\prime\prime}_{ax} + \frac{\mathcal{R}^{(1)\prime}_{ax}}{\tan\theta} + 2\mathcal{R}^{(1)}_{ax} - \cos\theta + \cos\theta_c + \frac{p_0^{(1)}}{\cos\alpha} = 0 \quad \text{with} \quad \mathcal{R}^{(1)\prime}_{ax}(0) = \mathcal{R}^{(1)}_{ax}(\theta_c) = 0, \tag{2.13}$$

$$\mathcal{R}^{(1)\prime\prime}_{nax} + \frac{\mathcal{R}^{(1)\prime}_{nax}}{\tan\theta} + \left(2 - \frac{1}{\sin^2\theta}\right)\mathcal{R}^{(1)}_{nax} + \sin\theta = 0 \quad \text{with} \quad \mathcal{R}^{(1)}_{nax}(0) = \mathcal{R}^{(1)}_{nax}(\theta_c) = 0. \tag{2.14}$$

The boundary conditions at $\theta = 0$ ensure that the interface is continuous and smooth. Also, $p_0^{(1)}$ is included in the equation for $\mathcal{R}^{(1)}_{ax}$ because it is invariant to changes in the tilt angle from α to $-\alpha$, which indicates that its value is proportional to $\cos\alpha$. The exact solutions of Eqs. 2.13 and 2.14 are, respectively,

$$\begin{aligned}\mathcal{R}^{(1)}_{ax}(\theta) &= \frac{1}{6}\left[\left(3\cos\theta_c + \frac{3p_0^{(1)}}{\cos\alpha} - 2\right)\left(\frac{\cos\theta}{\cos\theta_c} - 1\right) - 2\cos\theta\ln\left(\frac{1+\cos\theta}{1+\cos\theta_c}\right)\right] \\ &= \frac{1}{6}\left\{\cos\theta\left[1 - 2\ln\left(\frac{1+\cos\theta}{1+\cos\theta_c}\right)\right] - \cos\theta_c\right\},\end{aligned} \tag{2.15}$$

$$\mathcal{R}^{(1)}_{nax}(\theta) = \frac{1}{3}\left\{\sin\theta\left[\ln\left(\frac{1+\cos\theta}{1+\cos\theta_c}\right) - \tan\frac{\theta_c}{2}\cot\theta_c\right] + \tan\frac{\theta}{2}\cos\theta\right\}, \tag{2.16}$$

where

$$p_0^{(1)} = \frac{2}{3}\cos\alpha\,(1-\cos\theta_c)\,. \tag{2.17}$$

The first-order correction to the reference pressure is calculated by enforcing that the perturbations due to $\mathcal{R}^{(1)}$ do not alter the volume of the droplet. After some manipulations, this requirement simplifies to

$$\int_0^{\theta_c} \mathcal{R}^{(1)}_{ax}(\theta)\sin\theta\;\mathrm{d}\theta = 0. \tag{2.18}$$

Finally, we note that the preceding derivation can also be performed (with some additional steps) in a cylindrical coordinate system centered at $(x = 0, y = 0, z = 0)$ [35]. However, eventually a transformation to the spherical coordinates becomes necessary since overhangs and $\theta_c > \pi/2$ cannot be handled in that system.

2.3 Numerical solution based on energy minimization

The above perturbation solution is expected to be accurate for small Bond numbers. To cover a wider range of Bo, one could continue solving for higher-order corrections analytically, which is mathematically involved. Instead, we resort to numerical simulation. As mentioned earlier, the shape of the droplet can be determined, alternatively, by minimizing the Helmholtz free energy of the system, given the constraints

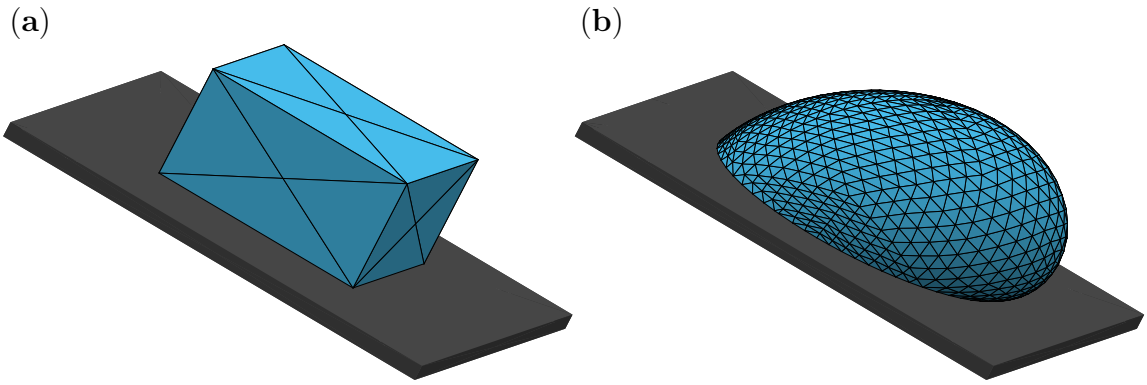

Figure 2.2: (a) Initial and (b) converged geometry of sessile drop from the *Surface Evolver* with parameters Bo = 5, $\theta_c = \pi/2$, and $\alpha = \pi/6$. For visualization purposes the discretized mesh shown in (b) is coarser than what was actually used in our numerical analyses.

of constant volume and pinned circular contact line. In fact, this approach is more amenable to numerical computation. We use the *Surface Evolver* [36] to numerically solve for the shape of the droplet, with no restriction on Bo as long as the results are physically meaningful. The *Surface Evolver* is a well-established computer program that minimizes the energy of a surface (which can take various forms) subject to constraints. Details of the implementation can be found in Refs. 36–38.

Provided with an initial simplified geometry (see Fig. 2.2a), geometrical constraints, and physical parameters, the 3D surface geometry of the perturbed drop is calculated by minimizing the Helmholtz free energy, following the negative energy gradient [36–38]. The initial geometry is discretized using a simplicial complex representation, which is refined after each iteration. This procedure continues for as many iterations as needed for the geometry to become sufficiently converged as shown in Fig. 2.2b.

As previously discussed, we need several initial parameters and conditions to be

defined before we can numerically compute the surface geometry of the sessile drop. The initial geometry is specified to be a rectangular prism of volume V (see Fig. 2.2a). The bottom surface of the prism is set to be coincident with the substrate and is given a no penetration boundary condition. The relationship to the pinned contact radius is also specified; that is the four nodes in contact with the substrate lie on the three phase contact line (a circle of radius R). Since the base area of the initial geometry is dependent on R, the height of the prism is determined by the volume of the drop (Eq. 2.5). Additionally, all new nodes generated from the mesh refinement that are coincident with the substrate, will also be constrained to the contact line.

For our fundamental analysis, we are only interested in the effects of the Bond number and inclination angle on the total rate of evaporation, hence we create a non-dimensional model of the sessile drop and set all non-pertinent parameters (R, γ, ρ) equal to one. Through the use of the *Surface Evolver*, we iteratively solve the energy minimization problem and refine the mesh characterizing the surface of the sessile drop resulting in a locus of points that can be used to create the 3D geometry.

For the purposes of comparison between our analytical and numerical models, we chose to explore the effects of three main parameters, Bo, α, and the volume of the drop. Since we are keeping R constant for all simulations, the volume of the drop is only dependent on θ_c (see Eq. 2.5), so we adjust this variable to change the drop volume, and hence will refer to θ_c for different drop volumes. We create and compare geometries using four values of α (0, $\pi/6$, $\pi/3$, and $\pi/2$), four θ_c ($\pi/6$, $\pi/3$, $\pi/2$, and

$2\pi/3$), and a series of Bo ranging from 0 to 80. In the following section, we discuss the results from our analysis as well as the comparison between them.

2.4 Results and discussion

In this chapter, we have analytically derived a first-order expression for the shape of a sessile drop from the Young-Laplace equation as a function of the Bond number Bo, the drop volume (i.e. θ_c), and the angle of inclination α. We have also numerically computed the geometry using an energy minimization method allowing us to compare the models for the surface geometry using identical conditions and constraints, to test the validity of our first-order expression for the drop shape. For the purposes of comparison, we use the 2D profile along the symmetry plane of the drop which provides the largest deviation in geometry.

Under trivial conditions, meaning Bo $= 0$, our first-order expression for the droplet shape exactly matches that of the numerical simulation. This expected result provides a useful baseline for further comparisons between our analytical and numerical models. Next, we want to test how the Bond number affects the shape of the drop before introducing any inclination to the substrate ($\alpha = 0$). The results from these tests can be seen in Fig. 2.3, where each column refers to a different θ_c (and hence a different drop volume), and each comparison plot represents the Bond number displayed under that plot.

In this and future figures displaying our results for the drop shape, the Bond

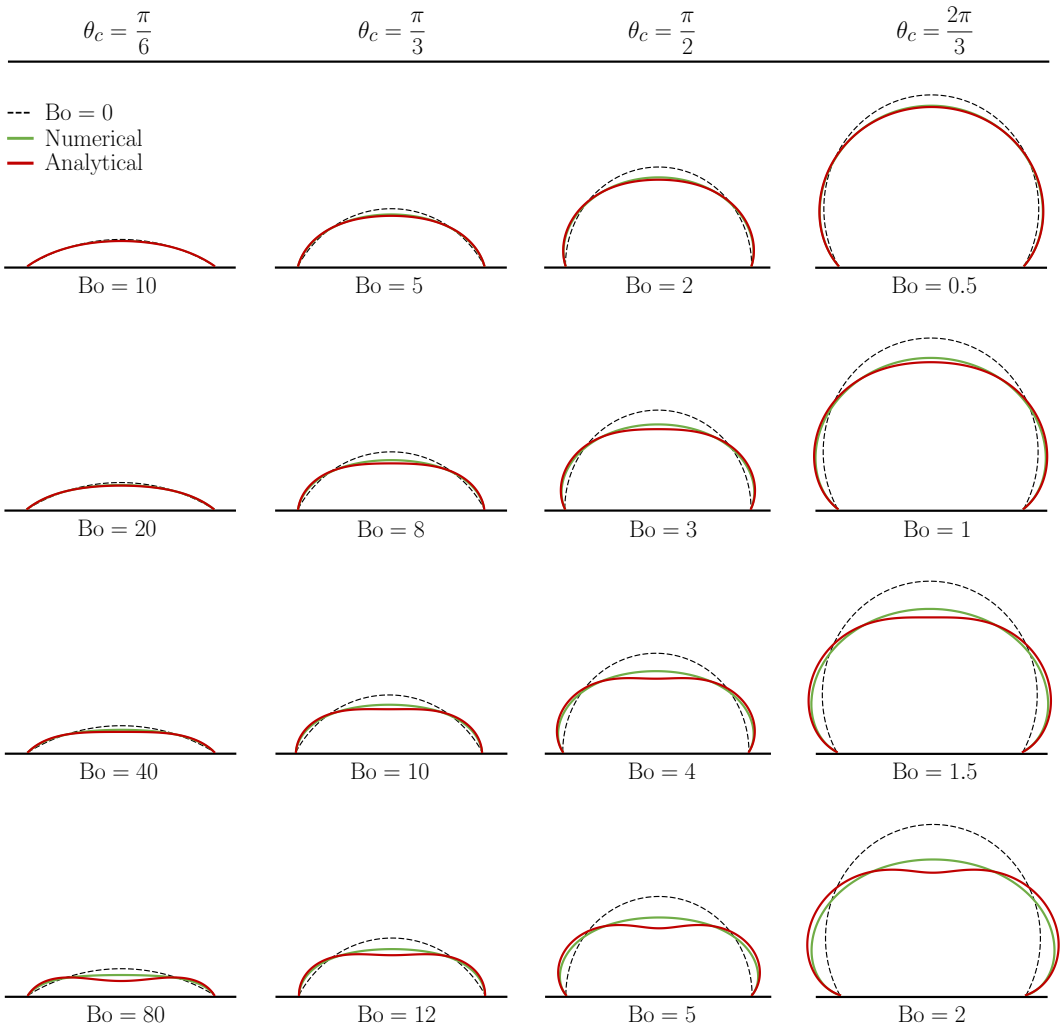

Figure 2.3: Center-line profiles of sessile drops for varying Bo and θ_c, while $\alpha = 0$ is constant.

number will generally increase in each successive row, allowing for easy visualization of trends. Additionally, the results from our numerical calculations, represented with the green solid lines, are shown along the predictions of the perturbation theory represented by the red solid lines. The comparisons in Fig. 2.3 clearly show that our first-order expression for the droplet shape near identically matches that of the numerical solution within our condition that the Bond number be small. Additionally,

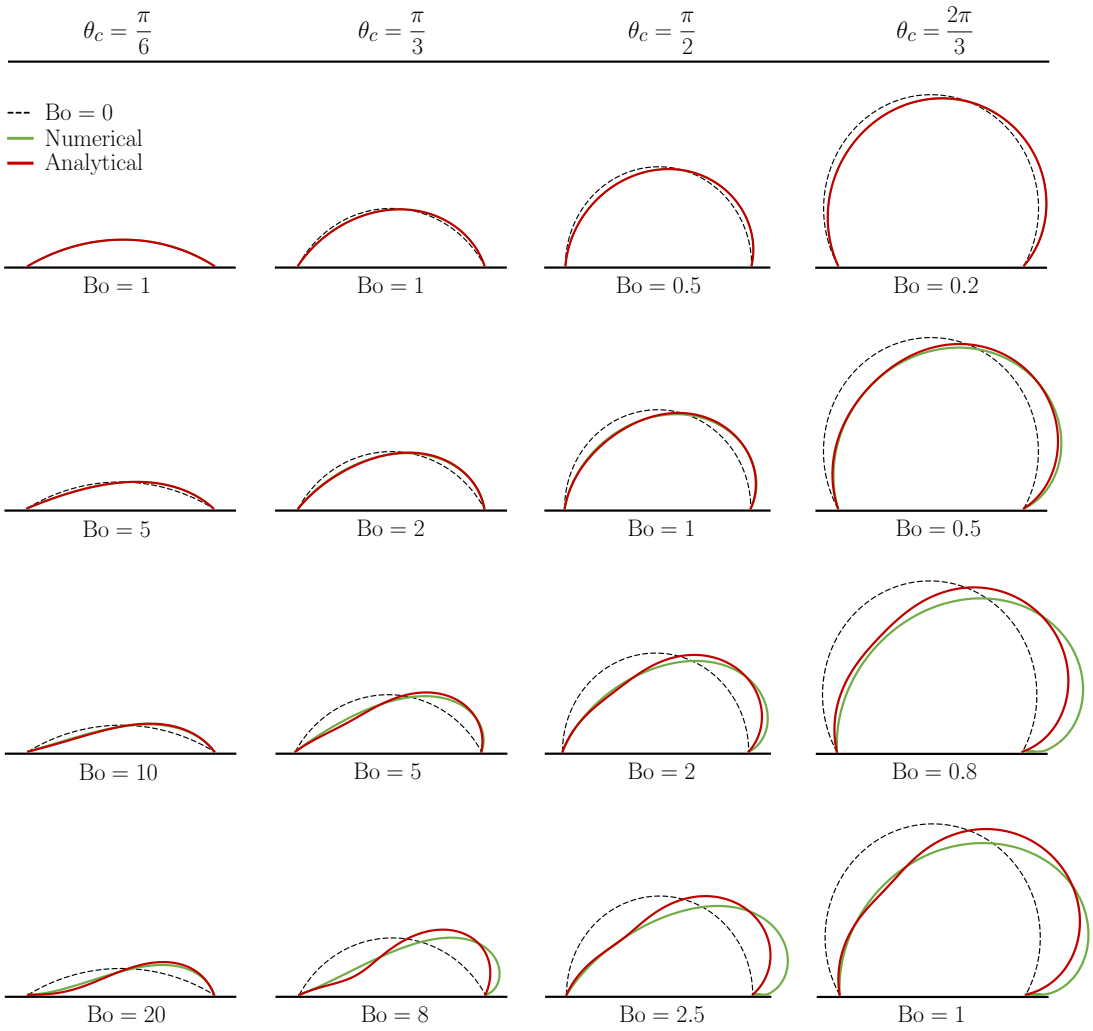

Figure 2.4: Center-line profiles of sessile drops for varying Bo and θ_c, while $\alpha = \pi/6$ is constant.

we surprisingly see high agreeance between our models of the drop shape outside the pre-set condition that Bo $\ll 1$, especially for small θ_c. However, the deviation between our analytical expression and the numerical solution expectedly increases with increasing Bond number. One may also notice that the first-order expression starts to deviate from the numerical solution at smaller Bond numbers as θ_c (or drop volume) increases. This shows us that the accuracy of our first order expression

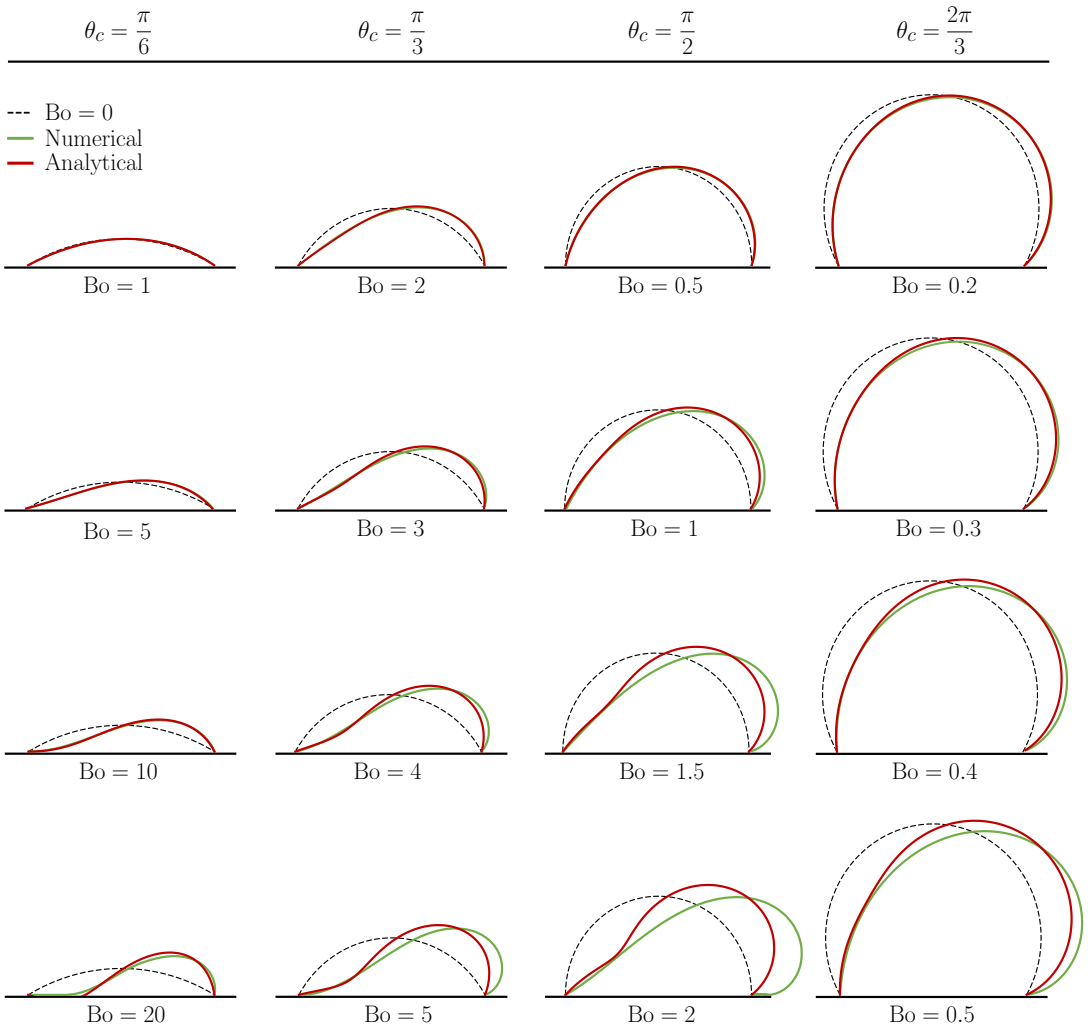

Figure 2.5: Center-line profiles of sessile drops for varying Bo and θ_c, while $\alpha = \pi/3$ is constant.

compared to the numerical solution is dependent on Bo as well as θ_c.

Now that we have an idea of what happens to the droplet shape under basic conditions ($\alpha = 0$), we want to see how the inclination angle affects the shape of the drop by increasing α to $\pi/6$. As can be seen in Fig. 2.4, there exists many of the same phenomena as in the case where $\alpha = 0$, e.g. high agreeance between models at small Bo and increasing deviation with increasing Bo and θ_c.

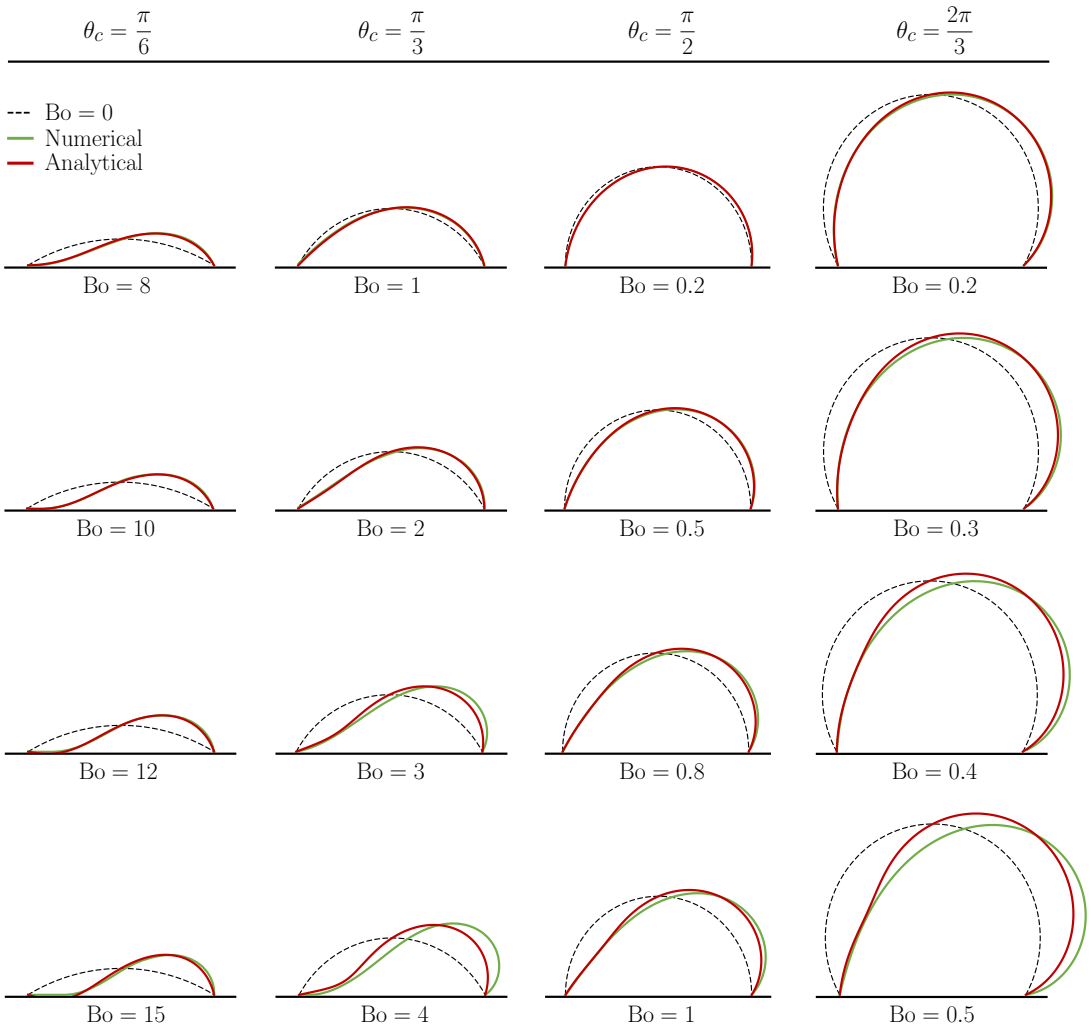

Figure 2.6: Center-line profiles of sessile drops for varying Bo and θ_c, while $\alpha = \pi/2$ is constant.

A key observation to be made, aside from the geometrical differences, is the Bo at which deviations between models start to occur. Increasing the angle of the slope seems to cause the first-order expression to deviate at smaller Bond numbers, e.g. when $\alpha = 0$ and $\theta_c = \pi/2$ our expression does not deviate until Bo $= 3$, meanwhile when $\alpha = \pi/6$ our expression deviates when Bo $= 2$. This trend can also be seen when α is increased to $\pi/3$ and $\pi/2$ in Fig. 2.5 and 2.6 respectively. These results

lead us to the conclusion that our first-order expression for the shape of a sessile drop is valid and accurate for sufficiently small Bo and α.

Chapter 3

Quasi-steady evaporation of a non-axisymmetric sessile droplet

3.1 Problem statement

Having discussed the shape of sessile drops under numerous conditions, we can now continue to show the impact of these varying geometries on the evaporation of a liquid droplet. In this chapter, we analytically derive the rate of evaporation using the expression for the droplet shape (Eq. 2.8a) previously obtained. Numerical simulation is then used to directly compare our results, testing the validity of the final expression. In our analysis, we assume that the evaporation is purely diffusive, and any effects due to advection are negligible.

Analogous to the derivation of the droplet shape in the previous chapter, we attain a dimensionless expression for the rate of evaporation in terms of Bo, utilizing

perturbation expansions. Ultimately, for us to determine the relationship between α and the total rate of evaporation J, we need to incorporate our model for the droplet shape, for which we know the relation to α. This is the main distinction between our work, and previous investigations, and is the reason we use the same coordinate space as the derivation of the drop shape (see Fig. 2.1c). In the following section, we analytically derive an expression for the total rate of evaporation J, starting from the Laplace equation. We show that including the first order model for the drop shape, coupled with Green's second identity, yield a surprisingly simple and concise formula.

To enhance and extend our analytical results, we numerically solve for the evaporation using a finite-volume method (FVM). The FVM simulations are intended as supplementation for comparison to our analytical expression for evaporation. As shown in Section §2.4, the numerical models for the droplet shape are much more stable at larger Bo, for this reason the numerical models are used in the FVM simulations. Since our derivation of J utilizes the analytical model for the droplet shape, we are able to observe the accuracy when compared to the numerical simulations of J at high Bo (outside the range of $\mathrm{Bo} \ll 1$). In Section §3.3, we detail the process, parameters, and conditions used in the numerical simulations.

In the last section, we show the results of the total rate of evaporation from both of the analytical and numerical methods. We asses the accuracy of the analytical expression for J by showing the relative error to our numerical simulations for the drop geometries obtained in the previous chapter. Finally, we present and discuss

the results and trends in J for the numerous parameters used to obtain the surface geometries.

3.2 Analytical solution using a perturbation theory

Having determined the equilibrium shape of the droplet, we are in a position to answer the question we posed in the introduction, which was about the effect of droplet deformation under gravity on how fast it evaporates. The rate at which the droplet loses mass is obtained by integrating the flux of the liquid vapor concentration in air over the free surface of the drop (denoted S_d), i.e.

$$J = -\int_{S_d} \boldsymbol{n} \cdot \boldsymbol{\nabla} c \, \mathrm{d}S, \tag{3.1}$$

where all the quantities are dimensionless. Specifically, the vapor concentration field c and total evaporation rate J are nondimensionalized by $c_s - c_\infty$ and $D\mathcal{R}_c(c_s - c_\infty)$, respectively. Here, c_s is the vapor concentration at S_d (saturation value), c_∞ is the far-field concentration, and D is the coefficient of binary diffusion of the vapor in air. We assume, as is routine, that the transport of the liquid vapor in the surrounding quiescent air is dominated by diffusion [21]. Hence, defining $\phi = c - c_\infty/(c_s - c_\infty)$, we have

$$\nabla^2\phi = 0 \quad \text{with} \quad \phi = 1 \text{ at } S_d, \quad \boldsymbol{n} \cdot \boldsymbol{\nabla}\phi \to 0 \text{ at } S_s, \quad \text{and} \quad \phi = 0 \text{ as } r \to \infty, \tag{3.2}$$

where S_s represents the surface of the substrate.

Given that S_d is described by $r = \mathcal{R} = 1 + \mathrm{Bo}\,\mathcal{R}^{(1)} + \mathcal{O}(\mathrm{Bo}^2)$, it is only natural to express the relative concentration field ϕ as

$$\phi = \phi^{(0)} + \mathrm{Bo}\,\phi^{(1)} + \mathcal{O}(\mathrm{Bo}^2), \tag{3.3}$$

which upon substitution into Eq. 3.2, yields

$$\nabla^2\phi^{(0)} = 0 \quad \text{with} \quad \boldsymbol{n}\cdot\boldsymbol{\nabla}\phi^{(0)} = 0 \text{ at } S_s \quad \text{and} \quad \phi^{(0)} \to 0 \text{ as } r \to \infty, \tag{3.4a}$$

$$\nabla^2\phi^{(1)} = 0 \quad \text{with} \quad \boldsymbol{n}\cdot\boldsymbol{\nabla}\phi^{(1)} = 0 \text{ at } S_s \quad \text{and} \quad \phi^{(1)} \to 0 \text{ as } r \to \infty, \tag{3.4b}$$

where the boundary conditions at S_d are omitted since an extra step is required to derive them. Consider a Taylor series expansion of ϕ about $r = 1$ as

$$\phi(r,\theta,\varphi) = \phi(1,\theta,\varphi) + (r-1)\left.\frac{\partial\phi}{\partial r}\right|_{r=1} + \ldots, \tag{3.5}$$

and apply the boundary condition $\phi(\mathcal{R},\theta,\varphi) = 1$, while replacing Eq. 3.3 for ϕ, to arrive at

$$\phi(r=\mathcal{R},\theta,\varphi) = \phi^{(0)}(1,\theta,\varphi) + \mathrm{Bo}\left[\phi^{(1)}(1,\theta,\varphi) + \mathcal{R}^{(1)}\left.\frac{\partial\phi^{(0)}}{\partial r}\right|_{r=1}\right] + \mathcal{O}(\mathrm{Bo}^2) = 1. \tag{3.6}$$

Requiring this equation to hold for each order of Bo, we find

$$\phi^{(0)}(1,\theta,\varphi) = 1 \qquad \text{and} \qquad \phi^{(1)}(1,\theta,\varphi) = -\mathcal{R}^{(1)}\left.\frac{\partial\phi^{(0)}}{\partial r}\right|_{r=1}, \tag{3.7}$$

which complete the boundary value problems in 3.4. Here, we have essentially converted the original boundary condition at S_d to a set of boundary conditions at the surface of the spherical cap $r = 1$, which we refer to hereafter as S_0.

To proceed, we also expand J in term of Bo as

$$J = J^{(0)} + \mathrm{Bo}\, J^{(1)} + \mathcal{O}(\mathrm{Bo}^2), \tag{3.8}$$

where

$$J^{(i)} = -\int_{S_d} \boldsymbol{n}\cdot\boldsymbol{\nabla}\phi^{(i)}\, \mathrm{d}S = -\int_{S_0} \boldsymbol{n}\cdot\boldsymbol{\nabla}\phi^{(i)}\, \mathrm{d}S \quad \text{with} \quad i = 0, 1. \tag{3.9}$$

The fact that S_d can be replaced with S_0 in the above surface integral directly results from having $\nabla^2\phi^{(i)} = 0$, everywhere in the domain including in the volume enclosed between S_0 and S_d. Laplace's equation 3.4a for $\phi^{(0)}$ can be solved exactly in a toroidal coordinate system that fits the boundary of the droplet using a special form of the method of separation of variables. Details of the derivation is available in Ref. 31. Thus, $\phi^{(0)}$ is already known, and so are its normal gradient at S_0 and its corresponding surface integral, which can be written in the forms

$$\begin{aligned}\boldsymbol{n}\cdot\boldsymbol{\nabla}\phi^{(0)}\big|_{S_0} = \left.\frac{\partial\phi^{(0)}}{\partial r}\right|_{r=1} &= -\frac{1}{2} - \frac{\sqrt{2}\sin^2\theta_c}{(\cos\theta - \cos\theta_c)^{3/2}} \\ &\times \int_0^\infty \frac{\cosh\theta_c\tau}{\cosh\pi\tau}\tanh\left[(\pi-\theta_c)\,\tau\right] P_{-1/2+i\tau}\left(\frac{1-\cos\theta\cos\theta_c}{\cos\theta-\cos\theta_c}\right)\tau\,\mathrm{d}\tau,\end{aligned} \tag{3.10a}$$

$$\begin{aligned}J^{(0)} &= -\int_0^{2\pi}\int_0^{\theta_c} \left.\frac{\partial\phi^{(0)}}{\partial r}\right|_{r=1} \sin\theta\,\mathrm{d}\theta\,\mathrm{d}\phi = -2\pi\int_0^{\theta_c} \left.\frac{\partial\phi^{(0)}}{\partial r}\right|_{r=1}\sin\theta\,\mathrm{d}\theta \\ &= \pi\sin\theta_c\left\{\frac{\sin\theta_c}{1+\cos\theta_c} + 4\int_0^\infty \frac{1+\cosh 2\theta_c\tau}{\sinh 2\pi\tau}\tanh\left[(\pi-\theta_c)\,\tau\right]\mathrm{d}\tau\right\},\end{aligned} \tag{3.10b}$$

where $P_{-1/2+i\tau}$ is the the conical function of the first kind, that can be evaluated via

$$P_\nu(\zeta) = \frac{1}{\pi}\int_0^\pi \left(\zeta + \cos\eta\sqrt{\zeta^2-1}\right)^{-(\nu+1)}\mathrm{d}\eta. \tag{3.11}$$

So, we are left to determine $J^{(1)}$.

If we were to follow the conventional approach, we would first solve Eq. 3.4b for $\phi^{(1)}$ and then integrate the associated flux over S_0 to obtain $J^{(1)}$. Here, however, we take an alternative approach that bypasses the elaborate task of solving for $\phi^{(1)}$ and directly calculates $J^{(1)}$. Consider multiplying Laplace's equation 3.4b by $\phi^{(0)}$ and Laplace's 3.4a by $\phi^{(1)}$, and then subtracting to reach

$$\phi^{(0)}\nabla^2\phi^{(1)} - \phi^{(1)}\nabla^2\phi^{(0)} = 0. \tag{3.12}$$

After adding and subtracting $\boldsymbol{\nabla}\phi^{(0)} \cdot \boldsymbol{\nabla}\phi^{(1)}$ and rearranging, this equation can be rewritten as

$$\boldsymbol{\nabla} \cdot \left(\phi^{(0)}\boldsymbol{\nabla}\phi^{(1)}\right) = \boldsymbol{\nabla} \cdot \left(\phi^{(0)}\boldsymbol{\nabla}\phi^{(0)}\right). \tag{3.13}$$

We now integrate Eq. 3.13 over the volume external to the drop and use the divergence theorem to obtain

$$\int_S \phi^{(0)}\, \boldsymbol{n} \cdot \boldsymbol{\nabla}\phi^{(1)}\, \mathrm{d}S = \int_S \phi^{(1)}\, \boldsymbol{n} \cdot \boldsymbol{\nabla}\phi^{(0)}\, \mathrm{d}S, \tag{3.14}$$

where S denotes all the surfaces bounding the distribution domain of $\phi^{(0)}$ and $\phi^{(1)}$, i.e. $S = S_0 + S_s + S_\infty$, with S_∞ representing a bounding surface at large distances. The above result is known as the Green's second identity and is the scalar version of the reciprocal theorem often used in solid and fluid mechanics [39]. It is also a special case of the reciprocal theorem developed by Vandadi et al. [40] for convective heat and mass transfer from particles in Stokes and potential flows.

Contributions from S_∞ to Eq. 3.14, vanish since both $\phi^{(0)}$ and $\phi^{(1)}$ decay at least as fast as $1/r$ as $r \to \infty$. Integrals over the substrate do not contribute either as

$\boldsymbol{n} \cdot \boldsymbol{\nabla}\phi^{(i)} = 0$ at S_s. Hence, applying Eqs. 3.7, we find

$$J^{(1)} = -\int_{S_0} \boldsymbol{n} \cdot \boldsymbol{\nabla}\phi^{(1)} \, \mathrm{d}S = \int_0^{2\pi} \int_0^{\theta_c} \mathcal{R}^{(1)} \left(\frac{\partial \phi^{(0)}}{\partial r}\bigg|_{r=1} \right)^2 \sin\theta \, \mathrm{d}\theta \, \mathrm{d}\varphi, \tag{3.15}$$

which, after incorporating eq 2.12 for $\mathcal{R}^{(1)}$, simplifies to

$$J^{(1)} = 2\pi \cos\alpha \int_0^{\theta_c} \mathcal{R}^{(1)}_{ax}(\theta) \left(\frac{\partial \phi^{(0)}}{\partial r}\bigg|_{r=1} \right)^2 \sin\theta \, \mathrm{d}\theta. \tag{3.16}$$

Note that the integral involving $\mathcal{R}^{(1)}_{nax}$ is zero because $\int_0^{2\pi} \cos\varphi \, \mathrm{d}\varphi = 0$.

3.3 Numerical solution via a finite volume method

Our solution for the evaporation is anticipated to be accurate to the leading order correction for the drop shape. To test the expected accuracy, we use numerical FVM simulations to generate results with which we can compare solutions. To conduct these simulations, we use the open-source CFD software *OpenFOAM*, which allows us to very precisely control the parameters used, the deiscretization of the surface, as well as define the solution method for our simulations.

The discretization of the surface geometry is a vital part of numerical analysis, and is worth mentioning in detail. The method used in our FVM simulations is different than that used previously in the *Surface Evolver*. Unlike the *Surface Evolver*, which uses a simplicial complex representation, *OpenFOAM* discretizes the surface of the droplets using a polygonal mesh [41]. This offers grater flexibility when it comes to the complex geometries which is present in asymmetric sessile drops, for there is no restriction on the number of edges on each polygonal element. The geometries used in

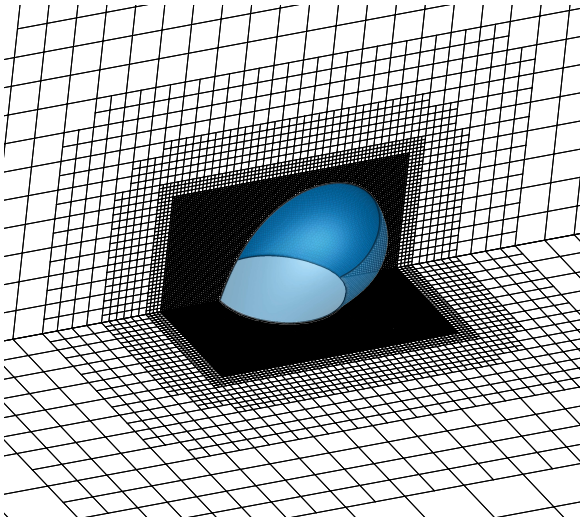

Figure 3.1: Example of a multi-block grid used for numerically solving Laplace's equation outside a sessile droplet (shown in blue). For clarity, only surface meshes on the symmetry plane and substrate are shown. The grid is generated by the *snappyHexMesh* utility of *OpenFOAM* [41], and coarsen as the distance from the free surface of the drop increases.

our FVM simulations are generated from the *Surface Evolver* since they are already discretized into a surface mesh with which we can create a solid form (see Figure 2.2b). Using the *Surface Evolver* geometries also allows us to conduct simulations for higher Bo, since the theoretical geometries become less accurate with increasing Bo. By running simulations for higher Bo (beyond the condition that $\mathrm{Bo} \ll 1$) we can find out the true limit for which our analytical model for the rate of evaporation is accurate.

The rate of evaporation is calculated by solving Laplace's equation (from our assumption of purely diffusive evaporation) for the vapor concentration field. Since we are only interested in the relative change of the evaporation (compared to $\mathrm{Bo} = 0$) at various α (for constant volume drops), we use a dimensionless model for evaporation in our numerical simulations. By setting the $c = 1$ at the droplet surface, $c = 0$ at the

far-field, and all other non-pertinent parameters such as diffusivity D and density ρ to one, we create a dimensionless model for evaporation that only depends on Bo and α. The outer boundary at infinity is modeled by a hemisphere of radius $100R$, whose center coincides with the center of the contact line circle. Given our large domain size, we use a multi-block mesh that is refined in the vicinity of the droplet to reduce the overall number of computational cells, while accurately resolving the gradients where they matter the most (see Figure 3.1). The smallest and largest grid spacings used are approximately $0.03R$ and $2R$, respectively. With all of the parameters and procedures described, we calculate the total rate of evaporation for the geometries previously generated. Implementation details of the FVM version used in *OpenFOAM* can be found in Ref. 41.

3.4 Results and discussion

As previously discussed, we expect our final solution for the total rate of evaporation to be accurate to the leading order correction to the drop shape. To test this, we compare the results for the total rate of evaporation from both our analytical solution and our numerical simulations. Just like our comparison of the droplet shapes, we use the same parameters (Bo, α, and θ_c) for the geometries in our analysis of the evaporation. Figure 3.2 shows the percentage difference between our analytical and numerical results for the total rate of evaporation.

These error plots show, under the condition that Bo $\ll 1$, our analytical solution

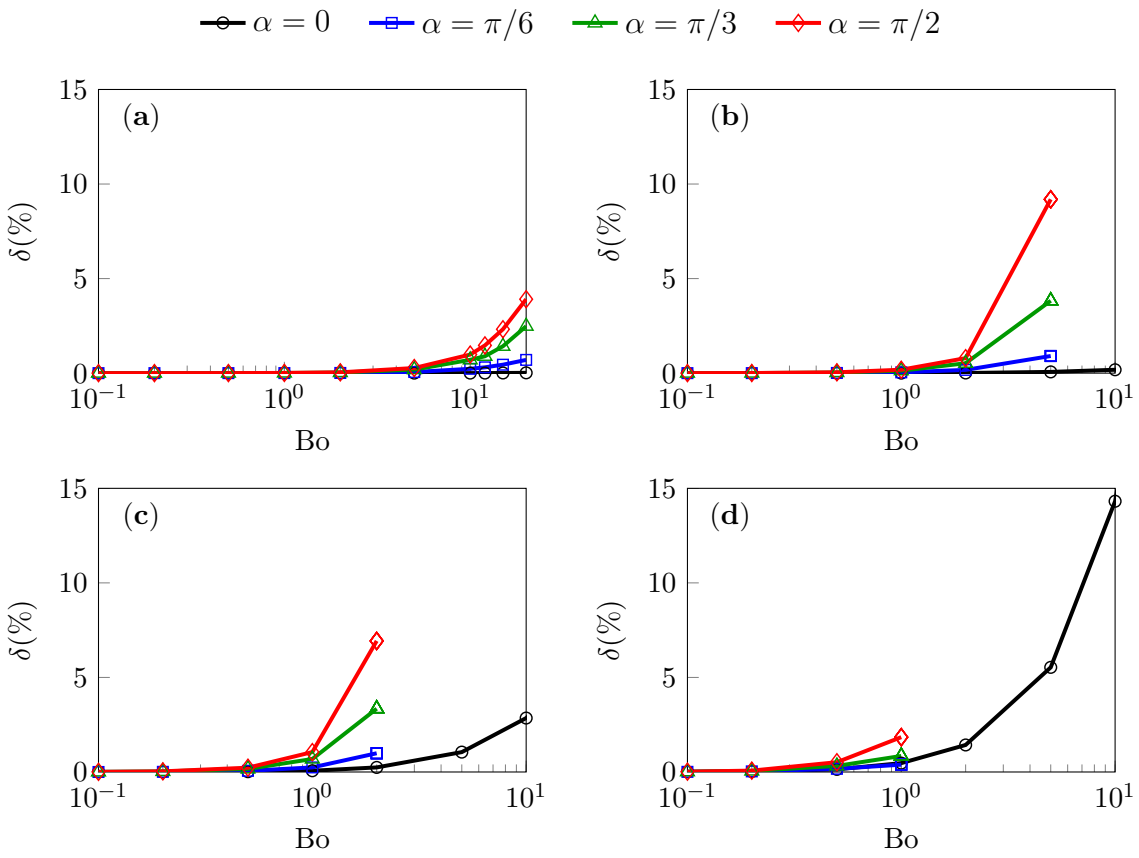

Figure 3.2: Percent difference δ between our analytical and numerical models for (a) $\theta_c = \pi/6$, (b) $\theta_c = \pi/3$, (c) $\theta_c = \pi/2$, and (d) $\theta_c = 2\pi/3$.

for the rate of evaporation closely matches that of our numerical simulations to within 3% (see Figure 3.2). Surprisingly, our expression is also shown to be valid for larger Bo as well (outside the Bo $\ll 1$ condition), or in the case of small θ_c (see Figure 3.2a) very large Bo. With this comparison validating our analytical expression, we can continue to show the results for the evaporation itself.

The results for the evaporation are presented in terms of dimensionless parameters. The evaporation is described as $J/J^{(0)}$ for any given Bo, α, and θ_c. With the results converted to dimensionless terms, we can observe the relative changes on the rate of

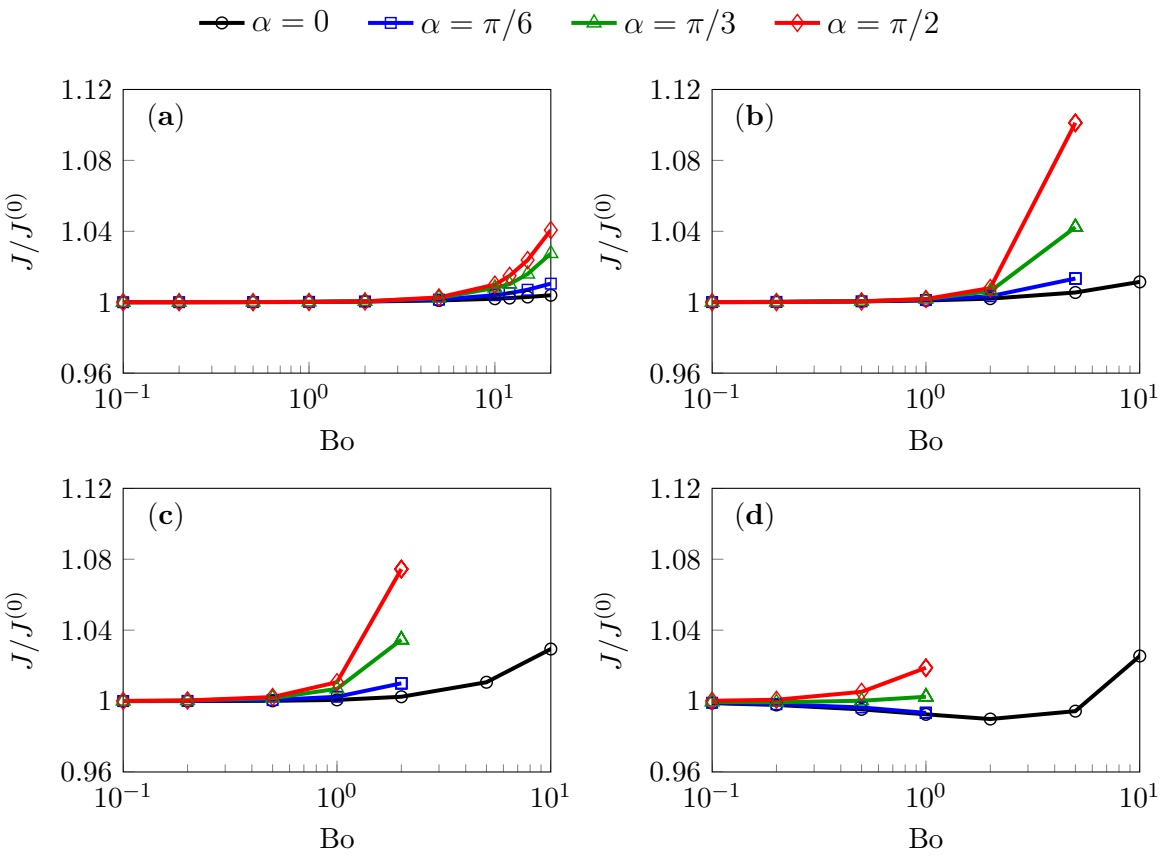

Figure 3.3: Normalized total rate of evaporation for (a) $\theta_c = \pi/6$, (b) $\theta_c = \pi/3$, (c) $\theta_c = \pi/2$, and (d) $\theta_c = 2\pi/3$.

evaporation with changing Bo and α. These results are presented in Figure 3.3 for various Bo, α, and θ_c.

Interestingly, we find that, at small Bo and α, the rate of evaporation experiences only minor fluctuations and remains almost unchanged despite having noticeable geometrical differences. We only start to see minor deviations (4–12%) in evaporation with larger Bo (i.e. Bo > 1). These results show, perhaps counter-intuitively, that the angle of inclination of the substrate (for a given Bo) does not have a significant impact on the evaporation rate.

Chapter 4

Summary and future directions

We have theoretically examined the evaporation of a sessile droplet pinned on an inclined surface, tilted to an angle α. Starting by finding the droplet shape, we analytically derived a first order expression from the Young-Laplace equation in terms of the Bond number, contact angle of the unperturbed droplet, and angle of inclination (Eq. 2.12). Using an energy minimization method, we numerically calculated the drop shapes for comparison to our analytical model. Final comparison between our analytical and numerical models (see Figs. 2.3-2.6) clearly show that our analytical model for the asymmetric drop shape very closely matches that of the numerical model for a wide range of Bond numbers, well beyond the expected limit of Bo $\ll 1$.

The total rate of evaporation, being the final goal of our analysis, was found in a similar fashion to the droplet shape, i.e. both analytical and numerical methods were used. Under the condition that Bo $\ll 1$, our analytical solution for the rate of evaporation very closely matches that of our numerical simulations. Additionally,

our expression is also shown to be valid for larger Bo as well (outside the Bo $\ll 1$ condition), or in the case of small θ_c, very large Bo. Remarkably, we find that, at small Bo and α, the rate of evaporation experiences only minor fluctuations and remains almost unchanged despite having noticeable geometrical differences. These results show, perhaps counter-intuitively, that the angle of inclination of the substrate does not have a significant impact on the total rate of evaporation. Furthermore, comparison between analytical and numerical calculations reveals that considering only the leading order corrections to the shape of the droplet and vapor concentration distribution provides estimates that are valid well beyond their intended limit of very small Bo.

After conducting the theoretical analysis presented in this paper, a few new areas of interest for future study arise. First of which is to find the leading order correction to the concentration field. The local flux of the concentration field is an important feature, and is needed to determine the boundary condition for the evaporation-induced fluid flow inside a sessile droplet (see e.g. [42, 43]). This is of interest when studying the deposition patterns of fully evaporated colloidal droplets (see e.g. [44]). With this further understanding, one could find the effect of the inclination angle on the so called *coffee-ring effect* (see e.g. [28]).

References

[1] Sirringhaus, H.; Kawase, T.; Friend, R. H.; Shimoda, T.; Inbasekaran, M.; Wu, W.; Woo, E. High-resolution inkjet printing of all-polymer transistor circuits. *Science* **2000**, *290*, 2123–2126.

[2] Bieri, N. R.; Chung, J.; Haferl, S. E.; Poulikakos, D.; Grigoropoulos, C. P. Microstructuring by printing and laser curing of nanoparticle solutions. *Appl. Phys. Lett.* **2003**, *82*, 3529–3531.

[3] Park, J.; Moon, J. Control of colloidal particle deposit patterns within picoliter droplets ejected by ink-jet printing. *Langmuir* **2006**, *22*, 3506–3513.

[4] Derby, B. Inkjet printing of functional and structural materials: fluid property requirements, feature stability, and resolution. *Annu. Rev. Mater. Res.* **2010**, *40*, 395–414.

[5] Galliker, P.; Schneider, J.; Eghlidi, H.; Kress, S.; Sandoghdar, V.; Poulikakos, D. Direct printing of nanostructures by electrostatic autofocussing of ink nanodroplets. *Nat. Commun.* **2012**, *3*, 890.

[6] Zhang, Z.; Zhang, X.; Xin, Z.; Deng, M.; Wen, Y.; Song, Y. Controlled inkjetting of a conductive pattern of silver nanoparticles based on the coffee-ring effect. *Adv. Mater.* **2013**, *25*, 6714–6718.

[7] Narayanan, S.; Wang, J.; Lin, X.-M. Dynamical self-assembly of nanocrystal superlattices during colloidal droplet evaporation by in situ small angle X-ray scattering. *Phys. Rev. Lett.* **2004**, *93*, 135503.

[8] Kuncicky, D. M.; Velev, O. D. Surface-guided templating of particle assemblies inside drying sessile droplets. *Langmuir* **2008**, *24*, 1371–1380.

[9] Byun, M.; Bowden, N. B.; Lin, Z. Hierarchically organized structures engineered from controlled evaporative self-assembly. *Nano Lett.* **2010**, *10*, 3111–3117.

[10] Ma, H.; Hao, J. Ordered patterns and structures via interfacial self-assembly: superlattices, honeycomb structures and coffee rings. *Chem. Soc. Rev.* **2011**, *40*, 5457–5471.

[11] Lin, Z. *Evaporative Self-Assembly of Ordered Complex Structures*; World Scientific: London, 2012.

[12] Han, W.; Lin, Z. Learning from "Coffee Rings": ordered Structures Enabled by Controlled Evaporative Self-Assembly. *Angew. Chem. Int. Ed.* **2012**, *51*, 1534–1546.

[13] Li, B.; Han, W.; Byun, M.; Zhu, L.; Zou, Q.; Lin, Z. Macroscopic highly aligned DNA nanowires created by controlled evaporative self-assembly. *ACS Nano* **2013**, *7*, 4326–4333.

[14] Li, P.; Li, Y.; Zhou, Z.-K.; Tang, S.; Yu, X.-F.; Xiao, S.; Wu, Z.; Xiao, Q.; Zhao, Y.; Wang, H.; Chu, P. K. Evaporative Self-Assembly of Gold Nanorods into Macroscopic 3D Plasmonic Superlattice Arrays. *Adv. Mater.* **2016**, *28*, 2511–2517.

[15] Zhao, M.; Yong, X. Modeling Evaporation and Particle Assembly in Colloidal Droplets. *Langmuir* **2017**, *33*, 5734–5744.

[16] Brutin, D.; Sobac, B.; Loquet, B.; Sampol, J. Pattern formation in drying drops of blood. *J. Fluid Mech.* **2010**, *667*, 85–95.

[17] Sobac, B.; Brutin, D. Desiccation of a sessile drop of blood: Cracks, folds formation and delamination. *Colloids Surf. A* **2014**, *448*, 34–44.

[18] Hoth, C. N.; Choulis, S. A.; Schilinsky, P.; Brabec, C. High Photovoltaic Performance of Inkjet Printed Polymer:Fullerene Blends. *Adv. Mater.* **2007**, *19*.

[19] Aernoutsa, T.; Aleksandrov, T.; Girotto, C.; Genoe, J.; Poortmans, J. Polymer based organic solar cells using ink-jet printed active layers. *Proc. R. Soc. Lond. A* **2008**, *92*, 033306.

[20] Girotto, C.; Rand, B. P.; Genoea, J.; Heremans, P. Exploring spray coating as a deposition technique for the fabrication of solution-processed solar cells. *Sol. Energy Mater Sol. Cells* **2009**, *93*, 454–458.

[21] Cazabat, A.-M.; Guena, G. Evaporation of macroscopic sessile droplets. *Soft Matter* **2010**, *6*, 2591–2612.

[22] Nguyen, T. A.; Nguyen, A. V.; Hampton, M. A.; Xu, Z. P.; Huang, L.; Rudolph, V. Theoretical and experimental analysis of droplet evaporation on solid surfaces. *Chem. Eng. sci.* **2012**, *69*, 522–529.

[23] Nguyen, T. A.; Nguyen, A. V. On the lifetime of evaporating sessile droplets. *Langmuir* **2012**, *28*, 1924–1930.

[24] Erbil, H. Y. Evaporation of pure liquid sessile and spherical suspended drops: A review. *Adv. Colloid Interface Sci.* **2012**, *170*, 67–86.

[25] Larson, R. G. Transport and deposition patterns in drying sessile droplets. *AIChE J.* **2014**, *60*, 1538–1571.

[26] Stauber, J. M.; Wilson, S. K.; Duffy, B. R.; Sefiane, K. On the lifetimes of evaporating droplets. *J. Fluid Mech.* **2014**, *744*.

[27] Espín, L.; Kumar, S. Sagging of evaporating droplets of colloidal suspensions on inclined substrates. *Langmuir* **2014**, *30*, 11966–11974.

[28] Du, X.; Deegan, R. D. Ring formation on an inclined surface. *J. Fluid Mech.* **2015**, *775*.

[29] Sáenz, P. J.; Wray, A. W.; Che, Z.; Matar, O. K.; Valluri, P.; Kim, J.; Sefiane, K. Dynamics and universal scaling law in geometrically-controlled sessile drop evaporation. *Nat. Commun.* **2017**, *8*, 14783.

[30] Kim, J. Y.; Hwang, I. G.; Weon, B. M. Evaporation of inclined water droplets. *Sci. Rep.* **2017**, *7*, 42848.

[31] Lebedev, N. N. *Special Functions and Their Applications*; Prentice-Hall, INC.: Englewood Cliffs, NJ, 1965.

[32] Popov, Y. O. Evaporative deposition patterns: spatial dimensions of the deposit. *Phys. Rev. E* **2005**, *71*, 036313.

[33] Fitzpatrick, R. *Theoretical Fluid Mechanics*; 2053-2563; IOP Publishing, 2017.

[34] O'Brien, S. B. G. On the shape of small sessile and pendant drops by singular perturbation techniques. *J. Fluid Mech.* **1991**, *233*, 519–537.

[35] De Coninck, J.; Dunlop, F.; Huillet, T. Contact angles of a drop pinned on an incline. *Phys. Rev. E.* **2017**, *95*, 052805.

[36] Brakke, K. A. The surface evolver. *Exp. Math.* **1992**, *1*, 141–165.

[37] Brakke, K. A. The Surface Evolver and the stability of liquid surfaces. *Phil. Trans. R. Soc. Lond. A* **1996**, *354*, 2143–2157.

[38] Brakke, K. A. Surface Evolver Manual. version 2.70, Mathematics Department, Susquehanna Univerisity: Selinsgrove, PA, USA, 2013.

[39] Masoud, H.; Stone, H. A. The Reciprocal Theorem in Fluid Dynamics and Transport Phenomena. *J. Fluid Mech.* **2019**, To be submitted.

[40] Vandadi, V.; Kang, S. J.; Masoud, H. Reciprocal theorem for convective heat and mass transfer from a particle in Stokes and potential flows. *Phys. Rev. Fluids* **2016**, *1*, 022001.

[41] Moukalled, F.; Mangani, L.; Darwish, M. *The Finite Volume Method in Computational Fluid Dynamics: An Advanced Introduction with OpenFOAM® and Matlab®*; Springer, 2015; Vol. 113.

[42] Masoud, H.; Felske, J. Analytical solution for inviscid flow inside an evaporating sessile drop. *Phys. Rev. E* **2009**, *79*, 016301.

[43] Masoud, H.; Felske, J. Analytical solution for Stokes flow inside an evaporating sessile drop: Spherical and cylindrical cap shapes. *Phys. Fluids* **2009**, *21*, 042102.

[44] Kang, S. J.; Vandadi, V.; Felske, J. D.; Masoud, H. Alternative mechanism for coffee-ring deposition based on active role of free surface. *Phys. Rev. E* **2016**, *94*, 063104.